International Journal for Uncertainty Quantification, 1 (3): 203–222 (2011)

RECONSTRUCTION OF DOMAIN BOUNDARY AND CONDUCTIVITY IN ELECTRICAL IMPEDANCE TOMOGRAPHY USING THE APPROXIMATION ERROR APPROACH

Antti Nissinen,[1] Ville Kolehmainen,[1,] & Jari P. Kaipio[2,1]*

[1] *Department of Applied Physics, University of Eastern Finland, P.O. Box 1627, FIN-70211 Kuopio, Finland*

[2] *Department of Mathematics, University of Auckland, Private Bag 92019, Auckland Mail Center, Auckland 1142, New Zealand*

Original Manuscript Submitted: 08/26/2010; Final Draft Received: 12/12/2010

Electrical impedance tomography (EIT) is a highly unstable problem with respect to measurement and modeling errors. With clinical measurements, knowledge about the body shape is usually uncertain. Since the use of an incorrect model domain in the measurement model is bound to lead to severe estimation errors, one possibility is to estimate both the conductivity and parametrization of the domain boundary. This could in principle be carried out using the Bayesian inversion paradigm and Markov chain Monte Carlo sampling, but such an approach would lead in clinical situation to an impractical solution because of the excessive computational complexity. In this paper, we adapt the so-called approximation error approach for approximate recovery of the domain boundary and the conductivity. In the approximation error approach, the modeling error caused by an inaccurately known boundary is treated as an auxiliary noise process in the measurement model and sample statistics for the noise process are estimated based on the prior models of the conductivity and boundary shape. Using the approximation error model, we reconstruct the conductivity and a low rank approximation for the realization of the modeling error, and then recover an approximation for the domain boundary using the joint distribution of the modeling error and the boundary parametrization. We also compute approximate spread estimates for the reconstructed boundary. We evaluate the approach with simulated examples of thorax imaging and also with experimental data from a laboratory setting. The reconstructed boundaries and posterior uncertainty are feasible; in particular, the actual domain boundaries are essentially within the posterior spread estimates.

KEY WORDS: *inverse problems, electrical impedance tomography, statistical inversion, modelling errors, inaccurately known boundary, model reduction*

1. INTRODUCTION

In electrical impedance tomography (EIT), electrodes are attached on the boundary of a body and electric currents are injected into the body through these electrodes. The resulting voltages on all electrodes are measured and the conductivity of the body is reconstructed based on the measured voltages and known currents. Mathematically, the problem amounts to estimating distributed parameters of an elliptic partial differential equation (PDE) based on a small number of measurement data on the boundary. The biomedical applications of EIT include detection of breast cancer [1, 2], imaging of brain function [3], and monitoring of lung function [4–6]. For reviews of EIT, see [7–9].

The reconstruction of the conductivity is an ill-posed problem; i.e., the problem is highly unstable with respect to measurement and modeling errors. The effect of the measurement errors can be reduced by using an accurate measurement system and by careful modeling of the statistics of the measurement errors. Modeling errors, on the

*Correspond to Ville Kolehmainen, E-mail: ville.kolehmainen@uef.fi, URL: http://venda.uku.fi/inverse/FrontPage/VilleKolehmainen

2152–5080/11/$35.00

other hand, are often related to model reduction, such as the use of coarse finite-element method (FEM) discretization of the forward model, truncation of the computational domain, or uncertainty in the values of nuisance parameters in the forward model, such as uncertainty in the values of model parameters that are assumed known.

In biomedical EIT, the most pivotal modeling error arises from inaccurate knowledge of the shape of the target body. The conventional setup for the EIT problem treats the boundary of the body as known. As an example, consider EIT measurements of pulmonary function from the surface of the thorax. In principle, the shape of the patient's thorax could be obtained from other imaging modalities such as computerized tomography (CT). However, such imaging data often are not available. Furthermore, the shape of the thorax varies in time due to breathing and is also dependent on the orientation of the patient. Therefore, the body shape—or the domain boundary in general—would be inaccurately known even at best. The use of an incorrect domain boundary in the measurement model has been shown to produce severe errors in the reconstructed conductivity images, see [10–13].

Since errors in the model domain lead to large reconstruction artifacts, one should in principle attempt to reconstruct both the conductivity and parametrization of the domain boundary. This could potentially be achieved, for example, by using the Bayesian inversion paradigm and Markov chain Monte Carlo sampling techniques. Once all the samples would be drawn, the marginalization of the posterior density model with respect to the nuisance parameters and computation of the estimates would be straightforward. However, such a sampling-based approach would be impractical in clinical use because of the excessive computational complexity and time—each sample would require solution of the FEM approximation of an elliptic PDE and construction of a FEM mesh for the domain corresponding to the drawn boundary parametrization. The reconstruction of the conductivity and a partially unknown boundary in an industrial process tomography application using an optimization-based approach has been considered in [14, 15]. However, the problem set up in these papers is significantly different compared to the present case and the methods would not be applicable as such. In these papers, the part of the boundary where the measurement electrodes are located (i.e., the walls of the process pipeline) are known and the only unknown boundary is the nearly flat air-liquid surface inside the process pipeline.

Instead of reconstructing both the conductivity and the domain boundary, there are a few distinct approaches to compensate for the errors caused by an inaccurately known boundary. A traditional (ad hoc) way for circumventing the problem of inaccurately known boundary has been to use difference imaging, where the objective is to reconstruct only the change in the conductivity between two measurement times (or two frequencies) using a first-order linear perturbation model [16]. The approach is highly approximative since the actual nonlinear forward mapping is approximated by a linear one and iterations are not possible in the first place. Furthermore, the choice of reconstructing conductivity differences based on differences of measurements is known to reduce the effect of an inaccurately known boundary only to an extent. In spite of the difference imaging modality being able to suppress some of the effects of model uncertainties, it has been shown that the breathing artifacts are still present in the reconstructions [17]. Furthermore, in high-contrast cases, such as accumulation of well conducting liquid (haematothorax) or poorly conducting air (pneumothorax) in the lungs, the linear approximation used in difference imaging may be insufficient for the detection of the clinically relevant conditions in the lungs [18]. Also, the detection of pneumothorax becomes difficult using difference imaging if the change in the lungs has occurred prior to the measurements [19].

Simultaneous reconstruction of the conductivity and electrode movement have been proposed for difference imaging in [20, 21]. These approaches are based on a linearized perturbation model and have been evaluated only for relatively small movements of the boundary between the measurement states. Recently, it has been demonstrated that the so-called D-bar method, which is a direct method based on a constructive uniqueness proof for two-dimensional (2D) EIT [22], has some tolerance against domain modeling errors [23]. The method proposed in [24, 25] eliminates the errors caused by an inaccurately known boundary in 2D EIT by using the theory of Teichmuller mappings. The method is based on the result that there is a unique anisotropic conductivity in the model domain that corresponds to the (noiseless) boundary data on the boundary of the true domain, and has minimal anisotropy. The numerical implementation of the method finds the minimally anisotropic conductivity by minimization of a regularized least-squares functional and displays the determinant of the anisotropic conductivity in the (incorrect) model domain as a deformed image of the original isotropic conductivity. The extension of the method to three-dimensional (3D) EIT was considered in [26]. For a discussion on the relation of the unknown boundary shape and anisotropic conductivities, also see [27].

In [28], we adapted the so-called approximation error approach for the compensation of the errors caused by an inaccurately known boundary in EIT. The approximation error approach is based on the Bayesian inversion paradigm. The key idea in the approximation error approach is, loosely speaking, to represent not only the measurement error, but also the effects of the computational model errors and uncertainties as an auxiliary additive noise process in the measurement model [29, 30]. The realization of the modeling error noise is obviously unknown since its value depends on the actual unknown conductivity and domain boundary. However, an approximation for the distribution of the modeling error can be estimated before the measurements using the prior probability distribution models of the conductivity and parametrization of the boundary. The estimated statistics are included (formally, by approximate marginalization) into the likelihood density to model the uncertainty in the measurement model caused by the uncertainty in the knowledge of the domain boundary. The approach was shown to remove efficiently the reconstruction artifacts caused by an inaccurately known boundary, producing deformed reconstructions of the target conductivity in the (incorrect) model domain.

The approximation error approach was originally developed and applied for discretization error in EIT with numerical examples in [29]. For this reason, the term "approximation error" also is commonly used where "modeling error" might be a more appropriate term. The approach was verified with real EIT data in [31], where the approach was employed for the compensation of discretization errors and the errors caused by an inaccurately known height of the air-liquid surface in an industrial mixing tank. The application of the approximation error approach for the discretization errors and the truncation of the computational domain was studied in [32], and for the linearization error in [33]. In [34] the approach was evaluated for the compensation of errors caused by coarse discretization, domain truncation, and unknown contact impedances with real EIT data. In addition to EIT, the approximation error approach has also been applied to other inverse problems and other types of (modeling) errors: Model reduction, domain truncation, and unknown anisotropy structures in optical diffusion tomography were treated in [35–38]. Missing boundary data in the case of image processing was considered in [39]. In [40], again related to optical tomography, an approximative physical model (diffusion model instead of the radiative transfer model) was used for the forward problem. In [41], an unknown uninteresting distributed parameter (scattering coefficient) was treated with the approximation error approach. The extension and application of the modeling error approach to time-dependent inverse problems was considered in [42–44].

In this paper, we propose an approach for reconstructing both the conductivity and the domain boundary. This is accomplished by employing the approximation error approach in a novel way. Instead of approximate marginalization over the modeling error, we split the modeling error noise process into two orthogonal components in the eigenvector basis of the estimated approximation error covariance, and then reformulate the EIT problem such that we also estimate, in addition to the conductivity, a low rank approximation for the realization of the modeling error in the basis formed by a few of principal eigenvectors. The estimate of the modeling error is then used to compute an approximation for the domain boundary based on approximate joint distribution of the modeling error and boundary shape parametrization. The approach is evaluated with simulated examples of thorax imaging as well as with measured EIT data from a chest-shaped laboratory tank. The results show that the approach gives feasible reconstruction of the conductivity and boundary shape when the target boundary is plausible with respect to the prior model for the boundary parametrization. Moreover, the posterior uncertainty estimates for the boundary shape are feasible.

The rest of this paper is organized as follows. In Section 2, a brief review of the EIT observation model, the Bayesian formulation of the EIT problem, and the approximation error approach is given. The practical construction of the approximation error method for the particular problem of an inaccurately known boundary shape is explained in Section 3. The proposed approach is evaluated using simulated 2D EIT data in Section 4 and with experimental EIT data in Section 5. Conclusions are given in Section 6.

2. METHODS

2.1 Forward Model of EIT and Notation

Let $\Omega \subset \mathbb{R}^d$, $d = 2, 3$, denote the measurement domain and let γ denote a parametrization of the domain boundary $\partial\Omega$. In an EIT experiment, a set of N_{el} contact electrodes are attached on the boundary $\partial\Omega$. Using the elec-

trodes, electric currents are injected into the body Ω and corresponding voltages are measured using the same electrodes.

We model these measurements with the so-called complete electrode model [45, 46]:

$$\nabla \cdot \sigma(x)\nabla u(x) = 0, \quad x \in \Omega \tag{1}$$

$$u(x) + z_\ell \sigma(x) \frac{\partial u(x)}{\partial n} = U_\ell, \quad x \in e_\ell \subset \partial\Omega, \tag{2}$$

$$\int_{e_\ell} \sigma(x) \frac{\partial u(x)}{\partial n}\, dS = I_\ell, \quad x \in e_\ell \subset \partial\Omega, \tag{3}$$

$$\sigma(x) \frac{\partial u(x)}{\partial n} = 0, \quad x \in \partial\Omega \setminus \bigcup_{l=1}^{N_{\mathrm{el}}} e_\ell. \tag{4}$$

where $x \in \mathbb{R}^d$, $u(x)$ is the potential distribution inside Ω, n is the outward unit normal vector at $\partial\Omega$, $\sigma(x)$ is the conductivity, and z_ℓ is the contact impedance between the object and the electrode e_ℓ. The currents satisfy the charge conservation law

$$\sum_{\ell=1}^{N_{\mathrm{el}}} I_\ell = 0, \tag{5}$$

and a ground level for the voltages can be fixed by

$$\sum_{\ell=1}^{N_{\mathrm{el}}} U_\ell = 0. \tag{6}$$

The numerical approximation of the forward model [Eqs. (1)–(6)] is based on the FEM approximation, see [8, 47]. In the following, we use notation $\sigma = (\sigma_1, \ldots, \sigma_N)^{\mathrm{T}} \in \mathbb{R}^N$ for the coefficients of the finite-dimensional representation

$$\sigma(x) = \sum_{k=1}^{N} \sigma_k \varphi_k(x) \tag{7}$$

in the FEM approximation (in this study, φ_k are the piecewise linear nodal basis functions of the FEM mesh) and

$$U(\sigma, \gamma) \in \mathbb{R}^m \tag{8}$$

for the FEM-based forward solution corresponding to a single EIT experiment; i.e., the vector $U(\sigma, \gamma)$ contains computed voltages for all the input currents in the chosen measurement paradigm. The dependence of the forward solution on the domain Ω is expressed by the parametrization γ of the boundary $\partial\Omega$. In the conventional setup for the EIT problem, the boundary parametrization γ plays the role of nuisance parameters. In the later sections, we consider only the modeling errors caused by inaccurately known domain boundary $\partial\Omega$ and approximate that mesh element size in the FEM mesh is chosen sufficiently small so that modeling errors caused by discretization are negligible.

The measurement noise in EIT experiments is commonly modeled as Gaussian additive noise that is mutually independent with the unknown conductivity. This leads to measurement model

$$V = U(\sigma, \gamma) + e, \quad e \sim \mathcal{N}(e_*, \Gamma_e) \tag{9}$$

where $V \in \mathbb{R}^m$ is the vector of the measured voltages, $\sigma \in \mathbb{R}^N$ and $e \in \mathbb{R}^m$ are Gaussian distributed measurement noise with mean $e_* \in \mathbb{R}^m$ and covariance matrix Γ_e.

Note that if boundary $\partial\Omega$ of the target body is not known accurately (realization of the nuisance parameters γ is incorrect), the error in the FEM approximation $U(\sigma, \gamma)$ may become significant compared to measurement error e. Together with the fact that the reconstruction of the conductivity is an ill-posed problem, this modeling error can easily lead to significant artifacts in the reconstructed conductivity.

2.2 Bayesian Approach for EIT Inverse Problem

In this section, the Bayesian framework for the EIT inverse problem is reviewed briefly. For more details of the Bayesian framework for inverse problems in general, see [8, 29, 48, 49], and the approximation error approach, in particular, for example [29, 30, 35, 41].

In the Bayesian framework, all unknowns and measurements are considered as random variables and the uncertainty related to their values is encoded in their probability distribution models. The joint probability density of conductivity σ, boundary parametrization γ, and measurements V can be written as

$$\pi(\sigma, \gamma, V) = \pi(\sigma, \gamma)\pi(V \mid \sigma, \gamma) = \pi(V)\pi(\sigma, \gamma \mid V), \tag{10}$$

where $\pi(V \mid \sigma, \gamma)$ is the *likelihood model* and the probability density $\pi(\sigma, \gamma)$ is the *prior model* of σ and γ. The posterior density, which is given by the Bayes formula

$$\pi(\sigma, \gamma \mid V) = \frac{\pi(V \mid \sigma, \gamma)\pi(\sigma, \gamma)}{\pi(V)}, \tag{11}$$

is the complete probabilistic model of the EIT problem and represents the uncertainty in the unknowns given the measurements.

In the conventional setup for the EIT problem, the domain boundary is assumed to be known. Let $\tilde{\Omega}$ denote an inaccurate model of the (actual) measurement domain Ω, and let $\tilde{\gamma}$ be a parametrization for boundary $\partial\tilde{\Omega}$. In the sequel, the tilde refers to the models that are to be used in the inversion. In the Bayesian formulation, all variables that are known, such as measurements, or *are treated as* fixed (nuisance) parameters, appear as conditioning variables. Thus, if we fix $\gamma = \tilde{\gamma}$, instead of $\pi(\sigma, \gamma \mid V)$ in Eq. (11), we actually consider

$$\pi(\sigma \mid V, \gamma = \tilde{\gamma}) = \frac{\pi(V \mid \sigma, \gamma = \tilde{\gamma})\pi(\sigma)}{\pi(V)} \tag{12}$$

Formally, the uncertainty in the primary interesting unknown σ is obtained by marginalization (integrating) over γ in Eq. (11)

$$\pi(\sigma \mid V) = \int \pi(\sigma, \gamma \mid V)\, d\gamma. \tag{13}$$

The posterior uncertainty of σ that is predicted by Eq. (12) is usually significantly overoptimistic when compared to the actual uncertainty given by Eq. (13). With this we mean that the density [Eq. (12)] tends to be significantly narrower than Eq. (13), and also most of the mass of the density [Eq. (12)] may be located differently than the mass of Eq. (13). In particular, any point estimates, such as the maximum a posteriori estimate, are bound to be highly misleading. It is clear that $\pi(\sigma \mid V) \neq \pi(\sigma \mid V, \gamma')$ generally with any γ'.

Unfortunately, the integral in Eq. (13) does not generally have an analytical solution and can be computed only with the often excessively resource demanding Markov chain Monte Carlo approach, see for example [29]. For this reason, approximations are usually needed to be considered in applications with limited computational resources.

Assuming that the conductivity and the boundary shape are mutually independent with the additive noise in Eq. (9), it follows that the likelihood can be written as

$$\pi(V \mid \sigma, \gamma) = \pi_e[V - U(\sigma, \gamma)], \tag{14}$$

where π_e is the probability density of noise e. In the following, we make a technical approximation that (σ, γ) are modeled as mutually independent so that $\pi(\sigma, \gamma) = \pi(\sigma)\pi(\gamma)$. Moreover, let the prior model be the Gaussian distribution $\mathcal{N}(\sigma_*, \Gamma_\sigma)$ equipped with the positivity constraint, so that we can write

$$\pi(\sigma) \propto \pi_+(\sigma) \exp\left[-\frac{1}{2}(\sigma - \sigma_*)^{\mathrm{T}}\Gamma_\sigma^{-1}(\sigma - \sigma_*)\right]$$

where $\sigma_* \in \mathbb{R}^N$ is the prior mean, Γ_σ is the prior covariance matrix, and $\pi_+(\sigma) = 1$ when all elements of σ are nonnegative, and zero otherwise.

Then, the posterior density of σ given *both* the measurements V *and* the nuisance parameters (boundary shape) γ becomes

$$\pi(\sigma \mid V,\gamma) \propto \pi_+(\sigma)\exp\left\{-\frac{1}{2}(\sigma-\sigma_*)^{\mathrm{T}}\Gamma_\sigma^{-1}(\sigma-\sigma_*)-\frac{1}{2}[V-U(\sigma,\gamma)-e_*]^{\mathrm{T}}\Gamma_e^{-1}[V-U(\sigma,\gamma)-e_*]\right\}. \quad (15)$$

Note that distribution (15) represents the posterior uncertainty in σ *only if* realization γ, which is used as a fixed parameter in Eq. (15), corresponds to the actual boundary.

In the Bayesian approach, the solution is analyzed and visualized by computing point and spread estimates for the posterior model [Eq. (15)], see for example [29]. In practical problems with restricted computational resources, the most commonly computed point estimate is the maximum a posteriori (MAP) estimate, which in the case of Eq. (15) leads to the following minimization problem:

$$\sigma_{\mathrm{MAP}} = \arg\max_{\sigma\ge 0}\pi(\sigma \mid V,\gamma) = \arg\min_{\sigma\ge 0}\left\{\|L_e[V-U(\sigma,\gamma)-e_*]\|^2+\|L_\sigma(\sigma-\sigma_*)\|^2\right\}, \quad (16)$$

where L_e and L_σ are Cholesky factors such that

$$\Gamma_e^{-1}=L_e^{\mathrm{T}}L_e, \quad \Gamma_\sigma^{-1}=L_\sigma^{\mathrm{T}}L_\sigma.$$

The minimization problem [Eq. (16)] can be solved, for example, by the Gauss-Newton algorithm [50]. We refer to the solution of Eq. (16) as the *MAP with conventional error model* (MAP-CEM). A computationally efficient approximation for the spread estimates (posterior covariance) can be obtained by forming a Gaussian approximation for the posterior density by linearization of the forward mapping $U(\sigma,\gamma)$ at the MAP-estimate σ_{MAP}, see [29]. Note that when Eq. (16) is computed, γ may or may not correspond to the actual boundary.

2.3 Reconstruction of the Conductivity and Domain Boundary Using the Approximation Error Approach

2.3.1 Measurement Models

Let

$$V = U(\bar{\sigma},\gamma)+e, \quad (17)$$

denote a (sufficiently) accurate model between the unknowns and measurements. Here, parameters γ of boundary $\partial\Omega$ are such that the error due to the FEM approximation is smaller than the measurement error. Conductivity $\bar{\sigma}$ is a parametrization in the actual Ω and is dense enough in the above sense.

As explained above, in practical clinical measurements one usually lacks accurate knowledge of the shape of body Ω and, therefore, the reconstruction is carried out using an approximate *model domain* $\tilde{\Omega}$. In such a case, the accurate model [Eq. (17)] is traditionally replaced by the approximate measurement model:

$$V \approx U(\sigma,\tilde{\gamma})+e, \quad (18)$$

where $\tilde{\gamma}$ is a parametrization of boundary $\partial\tilde{\Omega}$ of the model domain. It has been shown that the use of an incorrect model boundary $\partial\tilde{\Omega}$ produces significant errors to the conductivity estimates [11]. The model, $U(\sigma,\tilde{\gamma})$, in Eq. (18) is the forward model that is to be used in the inversion and we refer to model $U(\sigma,\tilde{\gamma})$ as the *target model*.

The relation of the representation of the conductivities in Eqs. (17) and (18) is of the form $\bar{\sigma}(x)=\sigma[T(x)]$, where

$$T(\Omega,\tilde{\Omega}) : \Omega \mapsto \tilde{\Omega} \quad (19)$$

is a bijective mapping that models the deformation of domain Ω to $\tilde{\Omega}$. Obviously, the true deformation, T, between the measurement domain and model domain is not unique and not known, and one has to choose a model for the deformation. The deformation of the conductivity can be represented by a linear transformation

$$P\bar{\sigma}=\sigma, \quad (20)$$

where $P(\Omega,\tilde{\Omega})$ is a matrix that interpolates the nodal conductivity $\sigma\in\mathbb{R}^N$ in Ω into a nodal conductivity in $\tilde{\Omega}$ according to deformation model T.

2.3.2 Approximation Error Model

In the approximation error approach, instead of writing the approximation [Eq. (18)], the *accurate measurement model* [Eq. (17)] is written in the form

$$V = U(\sigma,\tilde{\gamma}) + [U(\bar{\sigma},\gamma) - U(\sigma,\tilde{\gamma})] + e = U(\sigma,\tilde{\gamma}) + \varepsilon(\bar{\sigma},\gamma) + e = U(\sigma,\tilde{\gamma}) + \eta, \tag{21}$$

where we denote $\eta = \varepsilon + e$ and $\varepsilon(\bar{\sigma},\gamma)$ represents the modeling error due to the incorrect boundary, that is, the model discrepancy by using the incorrect boundary, $\partial\tilde{\Omega}$, instead of the correct one, $\partial\Omega$. Notice that only the term in Eq. (21), which depends on nuisance parameter γ, is approximation error ε.

Being a function of random variables, ε is a random variable and the joint density $\pi(\bar{\sigma},\varepsilon)$ can be computed in principle, but in most cases it does not have an analytical expression. Furthermore, in what follows, since we are to use variable σ in the inversion and $\sigma = P\bar{\sigma}$, we consider joint distribution $\pi(\varepsilon,\sigma)$.

In previous applications of the approximation error approach, the objective has been to derive a computationally efficient approximation $\tilde{\pi}(\sigma|V) \propto \tilde{\pi}(V|\sigma)\pi(\sigma)$ for posterior density $\pi(\sigma|V)$ based on the measurement model [Eq. (21)] and then use this model in the computations to compensate for the modeling errors. Since σ and γ are approximated as mutually independent, and the only term that depends on the random variable γ in Eq. (21) is η, the posterior model corresponding to Eq. (21) can be written as

$$\tilde{\pi}(\sigma|V) = \underbrace{\pi_{\eta|\sigma}[V - U(\sigma,\tilde{\gamma})|\sigma]}_{\pi(V|\sigma)}\,\pi(\sigma), \tag{22}$$

see [41] for details. A complication is that the likelihood, $\pi(V|\sigma)$, in Eq. (22) does not in general have an analytic expression. However, a computationally efficient approximation $\tilde{\pi}(V|\sigma)$ can be obtained by writing a Gaussian approximation for the joint density of (σ,η), and by conditioning over the nuisance parameter $\eta = e + \varepsilon$ we get the approximation for $\pi_{\eta|\sigma}$. This is the core of the implementation of the approximation error approach, in particular, when computational efficiency is sought. For further details, see [41].

2.3.3 Simultaneous Estimation of the Conductivity and Approximation Error

In this paper, we propose another way of utilizing the approximation error model in order to facilitate the approximate recovery of boundary $\partial\Omega$.

First, note that

$$\varepsilon - \varepsilon_* \in \mathrm{sp}\{w_1,\ldots,w_m\},$$

where $w_i \in \mathbb{R}^m$ are the mutually orthogonal eigenvectors of covariance matrix Γ_ε. Using this relation, we decompose the realization of the modeling error to mean plus two orthogonal components $(\varepsilon',\varepsilon'')$; that is, we write

$$\varepsilon = \varepsilon_* + \underbrace{\sum_{k=1}^{p}\alpha_k w_k}_{\varepsilon'} + \underbrace{\sum_{j=p+1}^{m}\beta_j w_j}_{\varepsilon''}. \tag{23}$$

Note that $\mathbb{E}(\varepsilon') = 0$ and $\mathbb{E}(\varepsilon'') = 0$. Formally, α_k and β_j are the projection coefficients $\alpha_k = \langle \varepsilon - \varepsilon_*, w_k\rangle$ and $\beta_j = \langle \varepsilon - \varepsilon_*, w_j\rangle$, respectively. In the following, we denote by $W = [w_1, w_2, \ldots, w_p]$ ($m \times p$ matrix) and $Q = [w_{p+1}, w_{p+2}, \ldots, w_m]$ ($m \times m - p$ matrix). Using Eq. (23), we write the measurement model [Eq. (21)] in the form

$$V = U(\sigma,\tilde{\gamma}) + \sum_{k=1}^{p}\alpha_k w_k + e + \varepsilon_* + \varepsilon'' = U(\sigma,\tilde{\gamma}) + W\alpha + \varepsilon_* + \varepsilon'' + e, \tag{24}$$

where $\alpha = (\alpha_1,\alpha_2,\ldots,\alpha_p)^{\mathrm{T}} \in \mathbb{R}^p$ and dimension p is chosen (significantly) smaller than m, so that ε' represents a low-rank projection of ε in the basis of principal eigenvectors of Γ_ε. By the properties of the eigenvalue decomposition, the prior distribution for the projection coefficients is $\alpha \sim \mathcal{N}(0,\Gamma_\alpha)$, where $\Gamma_\alpha = \mathrm{diag}(\lambda_1,\lambda_2,\ldots,\lambda_p)$ and λ_j

are the eigenvalues of Γ_ε. The dependence of the measurement model [Eq. (24)] on the boundary parametrization is embedded in the approximation error $\varepsilon = \varepsilon_* + W\alpha + \varepsilon''$.

Our objective now is to construct an approximation for the posterior density, $\pi(\sigma, \alpha|V)$, using the measurement model [Eq. (24)] and estimate both the conductivity and projection coefficients $\alpha \in \mathbb{R}^p$. To obtain a computationally efficient approximation, $\tilde{\pi}(\sigma, \alpha|V)$, we make the technical approximation that $(\sigma, \alpha, e, \varepsilon'')$ are mutually Gaussian and uncorrelated. Following the approach in [41], we obtain approximate likelihood

$$\tilde{\pi}(V|\sigma, \alpha) = \mathcal{N}(V - U(\sigma, \tilde{\gamma}) - W\alpha - \varepsilon_* - e_*, \Gamma_{\varepsilon''} + \Gamma_e)$$

and the approximate posterior density becomes

$$\tilde{\pi}(\sigma, \alpha \mid V) \propto \pi_+(\sigma) \exp\Bigg\{ -\frac{1}{2}(\sigma - \sigma_*)^{\mathrm{T}}\Gamma_\sigma^{-1}(\sigma - \sigma_*) - \frac{1}{2}\alpha^{\mathrm{T}}\Gamma_\alpha^{-1}\alpha - \frac{1}{2}[V - U(\sigma, \tilde{\gamma}) - W\alpha - \varepsilon_* - e_*]^{\mathrm{T}}$$
$$\times (\Gamma''_\varepsilon + \Gamma_e)^{-1}[V - U(\sigma, \tilde{\gamma}) - W\alpha - \varepsilon_* - e_*]\Bigg\}, \tag{25}$$

where $\Gamma_{\varepsilon''} = \sum_{p+1}^{m} \lambda_j w_j w_j^{\mathrm{T}}$.

The computation of the MAP estimate from the posterior model [Eq. (25)] amounts to solving the minimization problem

$$(\sigma, \alpha)_{\mathrm{MAP}} = \arg\min_{\sigma \geq 0, \alpha} \left\{ || \, L_{\varepsilon''+e}[V - U(\sigma, \tilde{\gamma}) - W\alpha - \varepsilon_* - e_*] \, ||^2 + || \, L_\sigma(\sigma - \sigma_*) \, ||^2 + || \, L_\alpha \alpha \, ||^2 \right\}, \tag{26}$$

where the Cholesky factor $L_{\varepsilon''+e}^{\mathrm{T}} L_{\varepsilon''+e} = (\Gamma_{\varepsilon''} + \Gamma_e)^{-1}$.

2.3.4 Reconstruction of the Boundary Shape

Once the MAP estimation problem [Eq. (26)] has been solved, an approximate estimate for boundary parameters γ of actual domain Ω are estimated. For this, we use the Gaussian approximation of the joint density of $\varepsilon' = W\alpha$ and γ and find the MAP estimate

$$\gamma_{\mathrm{MAP}} = \arg\max \tilde{\pi}(\gamma|\hat{\varepsilon}'), \tag{27}$$

given by

$$\hat{\gamma} = \Gamma_{\gamma\varepsilon'}\Gamma_{\varepsilon'}^{-1}\hat{\varepsilon}' + \gamma_*, \tag{28}$$

where $\hat{\varepsilon}' = W\alpha_{\mathrm{MAP}}$ and γ_* is the prior mean of the boundary parameters. Spread estimates for the boundary shape are obtained from the covariance of $\tilde{\pi}(\gamma|\hat{\varepsilon}')$, given by

$$\Gamma_{\hat{\gamma}|\hat{\varepsilon}'} = \Gamma_\gamma - \Gamma_{\gamma\varepsilon'}\Gamma_{\varepsilon'}^{-1}\Gamma_{\gamma\varepsilon'}^{\mathrm{T}}. \tag{29}$$

Note that the estimation [Eq. (26)] of conductivity σ and projection coefficients α is carried out in model domain $\tilde{\Omega}$. Once the MAP estimates of σ, α, and $\hat{\gamma}$ have been computed, the estimated conductivity, σ, is mapped from model domain $\tilde{\Omega}$ into the reconstructed domain, $\hat{\Omega}$ (that corresponds to MAP estimate $\hat{\gamma}$), by a linear interpolation

$$\hat{\sigma}_{\mathrm{MAP}} = \tilde{P}\sigma_{\mathrm{MAP}}, \tag{30}$$

where $\tilde{P}$ implements interpolation from the domain to another according to inverse T^{-1} of the domain deformation model [Eq. (19)]. We refer to the MAP estimate [Eqs. (26)–(30)] as the MAP with the *approximation error model* (MAP-AEM).

3. ESTIMATES AND CONSTRUCTION OF THE APPROXIMATION ERROR STATISTICS

In Section 4 we consider two test cases of 2D EIT with simulated measurement data and in Section 5 one 3D example with real measurement data from a laboratory experiment. In both the 2D and 3D cases the prior model is constructed similarly, and the approximation error statistics are computed likewise. In this section, we discuss these constructions with parameter values given for the 2D examples. The parameter values for the 3D cases are given in Section 5.

3.1 Estimates to Be Computed

Model domain $\tilde{\Omega}$ that is to be used in the inversion is circular with diameter ρ. For all test cases, the following reconstructions were computed:

1. σ_{MAP} with the conventional noise model [Eq. (16)] (MAP-CEM) in correct domain Ω [forward model $U(\bar{\sigma}, \gamma)$], this reconstruction serves as the reference reconstruction with the conventional measurement error model when no domain modeling errors are present.

2. MAP-CEM σ_{MAP} in model domain $\tilde{\Omega}$ [forward model $U(\sigma, \tilde{\gamma})$], representing conventional reconstruction in the presence of domain modelling errors.

3. MAP-AEM with the approximation error approach using model domain $\tilde{\Omega}$. We first compute $(\sigma_{\mathrm{MAP}}, \alpha_{\mathrm{MAP}})$ with Eq. (26) in $\tilde{\Omega}$ [forward model $U(\sigma, \tilde{\gamma}) + W\alpha$]. Given α_{MAP}, estimate $\hat{\gamma}$ of the boundary parametrization is computed using Eq. (28). The reconstructed conductivity σ_{MAP} is mapped from model domain $\tilde{\Omega}$ to reconstructed domain $\hat{\Omega}$ (that corresponds to estimate $\hat{\gamma}$) by mapping $\hat{\sigma}_{\mathrm{MAP}} = \tilde{P}\sigma_{\mathrm{MAP}}$ in Eq. (30).

The minimization problems [Eqs. (16) and (26)] were solved with the Gauss-Newton algorithm using a line search algorithm [50].

3.2 Prior Models

3.2.1 Prior Model for Conductivity

As the prior model $\pi(\sigma)$, we used a proper Gaussian smoothness prior, constructed similarly as in [29, 35, 36]. In the construction of the prior model, the conductivity is considered in the form

$$\sigma(x) = \sigma_{\mathrm{in}}(x) + \sigma_{\mathrm{hg}}(x)$$

where $\sigma_{\mathrm{in}}(x)$ is a spatially inhomogeneous conductivity with zero mean, and $\sigma_{\mathrm{hg}}(x)$ is a spatially homogeneous conductivity of nonzero mean. For the latter, we can write $\sigma_{\mathrm{hg}}(x) = c\mathbb{I}$, where $\mathbb{I}$ is a vector of ones and $\mathbb{R} \ni c \sim \mathcal{N}(\sigma_*, \mu_{\mathrm{hg}}^2)$. Setting the basis for conductivity, we have the coordinates $\sigma_{\mathrm{in}} \in \mathbb{R}^N$, $\mathbb{I} \in \mathbb{R}^N$, and set $\sigma_{\mathrm{in}} \sim \mathcal{N}(0, \Gamma_{\mathrm{in}})$. We model σ_{in} and c as mutually independent; that is, with respect to the prior model, the background conductivity is modeled mutually independent with the inhomogeneities in the conductivity.

For the homogeneous background, we set $\sigma_* = 2$ (arbitrary units) and $\mu_{\mathrm{hg}} = 0.5$. When constructing prior covariance Γ_{in}, we set the variance of elements (diagonal elements of Γ_{in}) to $\mu_{\mathrm{in}} = 1$, and the correlation length to $7\ \mathrm{cm}$. The correlation length roughly expresses our prior estimate about the expected size of the inhomogeneities in the medium. This also means that in the model for σ_{in}, any two elements that correspond to spatial locations that are further away from each other than the correlation length are (approximately) mutually independent.

Thus, we have the prior covariance $\Gamma_\sigma = \Gamma_{\mathrm{in}} + \mu_{\mathrm{hg}}^2 \mathbb{I}\mathbb{I}^{\mathrm{T}}$ and

$$\pi(\sigma) = \mathcal{N}(\sigma_* \mathbb{I}, \Gamma_\sigma).$$

This prior model is a proper distribution, in that the covariance exists in the first place. This model also allows (restricted) variation for the background (see Fig. 1).

Traditional smoothness prior models are improper, that is, the variances are infinite, and samples cannot be drawn from such distributions. The approximation error approach, on the other hand, is based on computing the statistics of ε over the prior distribution. This is not possible with a prior of unbounded variances.

3.2.2 Prior Model for Boundary Parametrization

As the prior model, $\pi(\gamma)$, we use a sample-based Gaussian approximation that is constructed based on an atlas of chest CT images of N_{pr} different individuals in the population. In this paper, we used an atlas of $N_{\mathrm{pr}} = 150$ images.

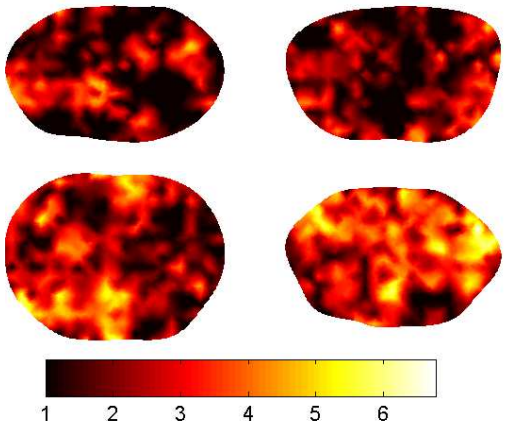

FIG. 1: Four 2D samples $\{\bar{\sigma}^{(\ell)}, \Omega^{(\ell)}\}$ for the construction of the approximation error model. The sample domains $\{\Omega^{(\ell)}\}$ are from an ensemble of chest CT images of different individuals and the conductivities are drawn from the prior model $\pi(\bar{\sigma})$. The unit of the 2D conductivity is arbitrary. The color scale denotes the common minimum to maximum scale of the conductivity values in the samples.

For this, the CT images were segmented to the interior and exterior of the body domain, leading to an ensemble of chest domains $\{\Omega^{(\ell)}, \ell = 1, 2, \ldots, N_{\rm pr}\}$. The domains were scaled so that the horizontal diameter is equivalent to diameter ρ of circular model domain $\tilde{\Omega}$. To obtain the corresponding parametric representations for the chest boundaries, $\{\partial\Omega^{(\ell)}\}$, we extracted boundaries $\{\partial\Omega^{(\ell)}\}$ from the scaled and segmented CT images and then employed a Fourier parametrization

$$b = \sum_{k=1}^{q} \gamma_k v_k = F\gamma, \tag{31}$$

for the representation of the boundaries. Here, vector b represents a set of points on the boundary, vectors v_k are the discretized sine and cosine functions on the unit circle, $F = [v_1, \ldots, v_q]$, and $\gamma \in \mathbb{R}^q$. In this paper, the number of sine and cosine functions was $q = 20$. This way, we obtained an ensemble $\{\gamma^{(\ell)}, \ell = 1, \ldots, N_{\rm pr}\}$ of parametric representations of chest shapes. Using the ensemble, the marginal prior model for γ was constructed as $\pi(\gamma) = \mathcal{N}(\gamma_*, \Gamma_\gamma)$, where

$$\gamma_* = \frac{1}{N_{\rm pr}} \sum_{k=1}^{N_{\rm pr}} \gamma^{(k)} \tag{32}$$

$$\Gamma_\gamma = \frac{1}{N_{\rm pr} - 1} \sum_{k=1}^{N_{\rm pr}} (\gamma^{(k)} - \gamma_*)(\gamma^{(k)} - \gamma_*)^{\rm T}. \tag{33}$$

This Gaussian approximation can be thought to reflect the natural variation in the chest shape in the population.

3.3 Estimation of Modeling Error Statistics

In cases in which the measurement model is linear and the prior model is Gaussian, the approximation error statistics can be computed analytically, see [29]. In other cases, the statistics typically are estimated by Monte Carlo simulation.

For the Monte Carlo simulation, we generate a set of N_s draws from prior models $\pi(\gamma)$ and $\pi(\bar{\sigma})$. In both the simulation and real data cases, $N_s = 1000$ random draws $\{\gamma^{(\ell)}, \bar{\sigma}^{(\ell)}\}$ were used for the estimation of joint sample statistics for (ε, γ). Using boundary parameter sample $\gamma^{(\ell)}$, a FEM mesh was automatically created using the MATLAB and Comsol mesh generators for sample domain $\Omega^{(\ell)}$ for computation of accurate model $U(\bar{\sigma}^{(\ell)}, \gamma^{(\ell)})$. Conductivity sample $\bar{\sigma}^{(\ell)}$ in sample domain $\Omega^{(\ell)}$ was drawn from the smoothness prior model, which was constructed

as in Section 3.2. To simplify the sampling process, model $\pi(\bar{\sigma})$ was defined on a FEM mesh in the rectangular domain that encloses all sample domains $\{\Omega^{(\ell)}\}$. To create sample $\bar{\sigma}^{(\ell)}$, a random sample was then drawn from $\pi(\bar{\sigma})$ in the rectangular domain and interpolated into nodal values $\bar{\sigma}_i$ in sample domain $\Omega^{(\ell)}$ [see Eq. (7)]. Figure 1 shows four samples $\{\bar{\sigma}^{(\ell)}\}$ on sample domains $\{\Omega^{(\ell)}\}$. The samples were then used for the computation of accurate forward solution $U(\bar{\sigma}^{(\ell)}, \gamma^{(\ell)})$ for each of the N_s samples.

To compute the target model, $U(\sigma^{(\ell)}, \tilde{\gamma})$, the conductivity samples were mapped from $\Omega^{(\ell)}$ to model domain $\tilde{\Omega}$ by

$$\sigma^{(\ell)} = P^{(\ell)}\bar{\sigma}^{(\ell)}, P^{(\ell)} : \Omega^{(\ell)} \mapsto \tilde{\Omega},$$

where $P^{(\ell)} = P^{(\ell)}(\Omega^{(\ell)}, \tilde{\Omega})$ is a matrix that interpolates nodal conductivity from $\Omega^{(\ell)}$ to $\tilde{\Omega}$ according to deformation T [see Eqs. (19)–(20)]. In the numerical examples considered in this study, T is chosen such that the angle and relative distance (between the center of the domain and the boundary) of a coordinate point is preserved. Although this simple deformation model seems to work well with the test cases we have considered, we note that other transformation models may be used as well. More advanced choices for the transformation model can be sought for from the literature of image registration, see e.g. [51].

Given the accurate and target forward solutions, samples $\varepsilon^{(\ell)}$ of the approximation error were obtained as

$$\varepsilon^{(\ell)} = U(\bar{\sigma}^{(\ell)}, \gamma^{(\ell)}) - U(\sigma^{(\ell)}, \tilde{\gamma})$$

The means and covariances, ε_*, γ_*, Γ_ε, $\Gamma_{\varepsilon''}$, $\Gamma_{\varepsilon'}$ and $\Gamma_{\gamma\varepsilon'}$, for the Gaussian approximations were computed as sample averages based on the samples, $\{\varepsilon^{(\ell)}, \gamma^{(\ell)}, \ell = 1, \ldots, 1000\}$. For this task, samples $\varepsilon^{'(\ell)}, \varepsilon^{''(\ell)}$ of the projection components were obtained from samples $\{\varepsilon^{(\ell)}\}$ by

$$\varepsilon^{'(\ell)} = WW^{\mathrm{T}}(\varepsilon^{(\ell)} - \varepsilon_*), \quad \varepsilon^{''(\ell)} = QQ^{\mathrm{T}}(\varepsilon^{(\ell)} - \varepsilon_*),$$

where ε_* is the sample average.

Note that the estimation of the approximation error statistics by Monte Carlo simulation is a computationally extensive task. However, this task can be done offline before the measurements and needs to be done only once for a given measurement setup, and for the expected range of uncertainties—in this paper, the range of boundary shapes and the specified prior model for the conductivity.

4. TEST CASES WITH SIMULATED DATA AND 2D FEM MODEL

4.1 Target Conductivity and Simulation Parameters for Cases 1 and 2

The actual thorax domain Ω and the target conductivity σ_{true} for the simulation examples (Cases 1 and 2) are shown in Fig. 3. The thorax domains as well as the subdomains for the lungs and the heart were obtained from two segmented CT reconstructions of the human thorax. Note that ensemble $\{\partial\Omega^{(\ell)}\}$ of the CT-based chest boundaries that was used to construct the prior model $\pi(\gamma)$ did not include either of these particular CT samples. The horizontal diameter of domains Ω was scaled to $\rho = 35\,\mathrm{cm}$, which is also used as the diameter of circular model domain $\tilde{\Omega}$ (see Fig. 3).

The true measurement domains also are shown together with the boundaries corresponding to the prior mean and two standard deviation limits in the sample-based Gaussian prior model, $\pi(\gamma)$, in Fig. 2. The solid line shows mean boundary $F\gamma_*$, see (31), and the dashed lines show the two standard deviation limits around the mean [the standard deviations are obtained as $\sqrt{\mathrm{diag}(F\Gamma_\gamma F^{\mathrm{T}})}$]. Notice that in the first simulation (Case 1), the true measurement domain lies mainly inside the two standard deviation limits of prior model $\pi(\gamma)$, whereas the measurement domain in Case 2 is clearly outside the two standard deviation limits of the prior model. Thus, Case 2 represents a difficult case since the actual measurement domain has a small probability with respect to prior model $\pi(\gamma)$.

In both cases, 16 equally spaced measurement electrodes were modeled on boundary $\partial\Omega$. The locations of the electrodes and the locations of the lungs and the heart are indicated in Fig. 3. The target conductivities were set to 1.2, 2, and 3.6 (arbitrary units) for the lungs, background, and heart, respectively. In the simulation of the EIT measurements, 16 adjacent current patterns were used and the voltages were measured between adjacent electrode pairs, leading to 256 voltage measurements; that is, $V \in \mathbb{R}^{256}$. The simulated measurements were computed with

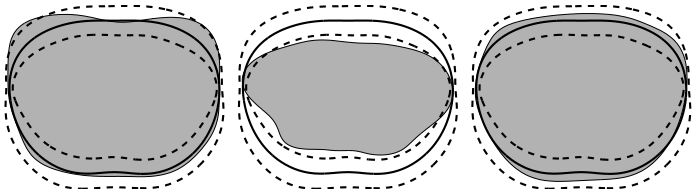

(Case 1) (Case 2) (Case 3)

FIG. 2: The actual measurement domains Ω are shown as gray patch. Cases 1 & 2 are the test cases with simulated measurement data and case 3 is the example with measurement data from a laboratory experiment. The solid line shows the boundary corresponding to mean γ_* of prior model $\pi(\gamma)$ and dashed line shows the 2 standard deviation limits of $\pi(\gamma)$.

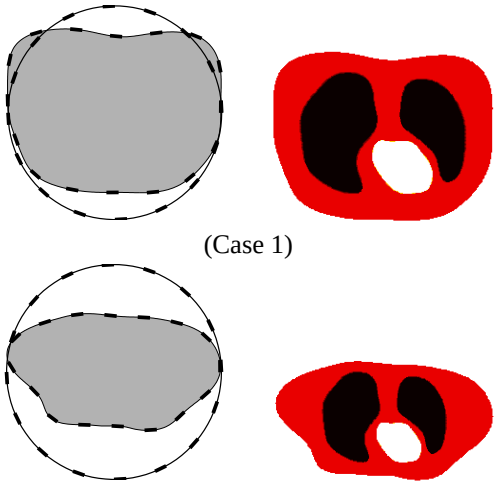

(Case 1)

(Case 2)

FIG. 3: Left: The actual measurement domains Ω are shown as gray patch. The circular model domain $\tilde{\Omega}$ is shown by solid line. The locations of the 16 electrodes on the boundaries $\partial\Omega$ and $\partial\tilde{\Omega}$ are shown with thick line segments. Right: Arrangement of lungs and heart in the actual domains.

2D FEM approximation. To avoid an "inverse crime,"[1] the simulated measurement data were generated using a finer discretization level than is used in the inverse problem computations. Further, Gaussian mutually independent noise was added to the simulated measurements. The added noise, e, was zero mean and the standard deviation of the noise was 1% of the computed simulated voltages corresponding to the signal-to-noise ratio, SNR = 40 dB.

4.2 Reconstructions for Cases 1 and 2

In the present implementation, one tuning parameter is dimension p of parameter vector $\alpha \in \mathbb{R}^p$, which defines the dimension of projection component ε' [see Eq. (23)]. To find a suitable p, we seek the smallest p such that $\mathrm{var}\|e\| = \mathrm{tr}(\Gamma_e) > \mathrm{tr}(\Gamma_{\varepsilon''}) = \mathrm{var}\|\varepsilon''\|$. The rationale behind this choice is to find a level where the magnitude of residual modeling error ε'' gets smaller than the magnitude of random measurement noise e. We found that this criterion was met with $p = 32$, which is used in the following. To verify the sensibility of this choice, we computed MAP-AEM reconstructions [Eqs. (26)–(30)] for Case 1 using different values of p in the range $p \in [3,\ 100]$. Reconstructed domain and conductivity for values $p \in \{3, 10, 30, 60, 100\}$ are shown in Fig. 4. As can be seen, the (visual) quality of the

[1]Inverse crime refers to an overly optimistic test setting where an identical forward model is used for both simulation of the measurement data and in the inverse problem.

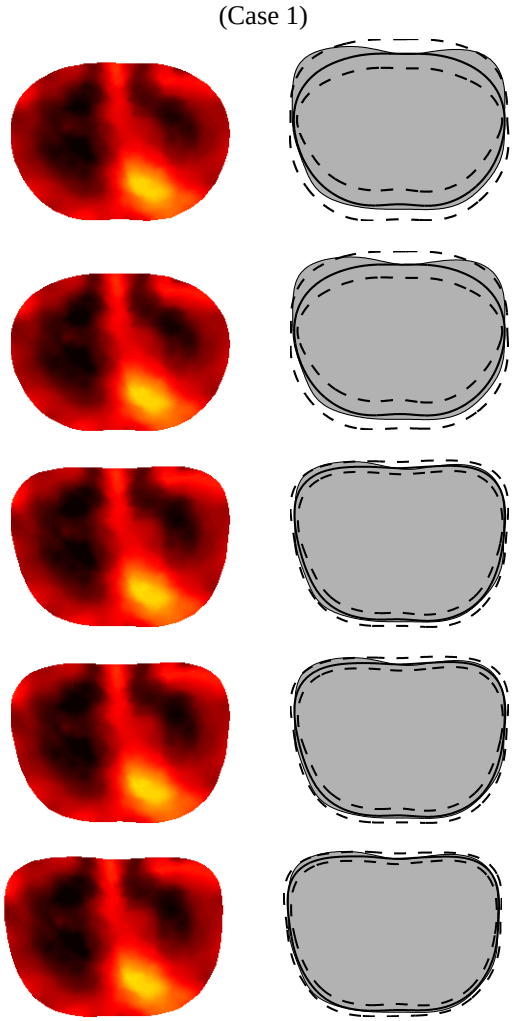

FIG. 4: MAP-AEM reconstructions $\hat{\sigma}_{\mathrm{MAP}}$ with different dimension of parameter vector $\alpha \in \mathbb{R}^p$ (see 23 and 26). The right column shows the reconstructed boundary $F\hat{\gamma}$ with solid line and the *a posteriori* two standard deviation limits for the approximate posterior $\tilde{\pi}(\gamma|\hat{\varepsilon}')$ [the standard deviation limits are obtained as $\sqrt{\mathrm{diag}(F\Gamma_{\hat{\gamma}|\hat{\varepsilon}'}F^{\mathrm{T}})}$]. The values of p are from top to bottom: 3, 10, 30, 60 and 100.

estimate does not improve once p exceeds the level where ε'' gets smaller than noise e, giving support to our choice of dimension p for projection component ε'.

The reconstructions of Type 1–3 described in Section 3.1 are shown for Case 1 in Fig. 5. The top left shows the target conductivity, σ_{true}, the top right show the MAP-CEM estimate using correct domain Ω, the middle left shows the MAP-CEM using incorrect model domain $\tilde{\Omega}$, and the middle right show the MAP-AEM estimate $\hat{\sigma}_{\mathrm{MAP}}$, which was computed using the same incorrect model domain $\tilde{\Omega}$. The bottom row shows the reconstructed boundary $F\hat{\gamma}$ with a solid line, two standard deviation limits for posterior $\tilde{\pi}(\gamma|\hat{\varepsilon}')$ with a dashed line, and true measurement domain Ω with a gray patch. The relative estimation errors

$$\Delta_\sigma = \frac{\| P\sigma_{\mathrm{true}} - \sigma \|}{\| P\sigma_{\mathrm{true}} \|} \cdot 100\% \,, \tag{34}$$

for the estimates are listed in Table 1.

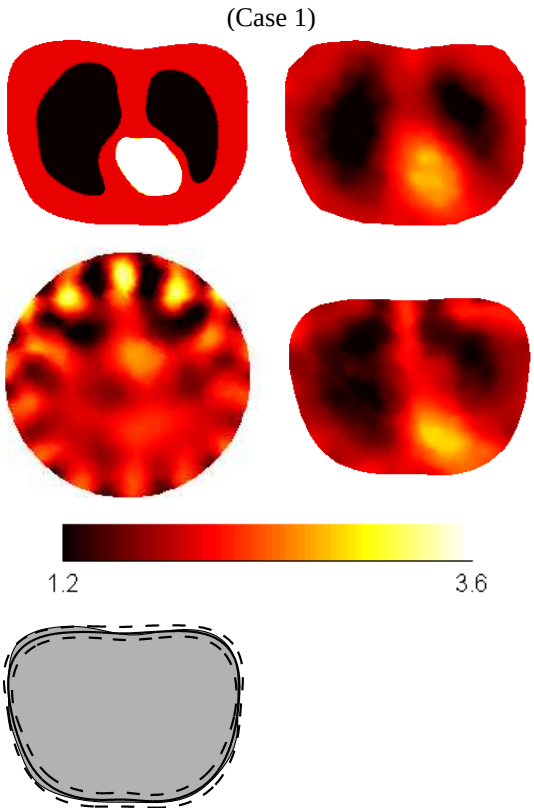

FIG. 5: Top left: Actual conductivity σ_{true}. Top right: MAP-CEM estimate using the correct domain Ω. Middle left: MAP-CEM using the incorrect model domain $\tilde{\Omega}$. Middle right: MAP-AEM using the incorrect model domain $\tilde{\Omega}$. Bottom: The actual domain Ω is shown as gray patch. The reconstructed boundary is shown with solid line and 2 (*a posteriori*) standard deviation limits with dashed lines.

TABLE 1: The relative estimation errors (Case 1).

Estimate	Forward model	Δ_σ
MAP-CEM	$U(\bar{\sigma},\gamma)$	19.63
MAP-CEM	$U(\sigma,\tilde{\gamma})$	37.56
MAP-AEM	$U(\sigma,\tilde{\gamma})$	19.67

The MAP-CEM with accurate forward model $U(\bar{\sigma},\gamma)$ using correct measurement domain Ω can be taken as a reference estimate. The error in the estimate is due to the ill-posed nature of the EIT problem. We note, however, that the particular prior model $\pi(\bar{\sigma})$, which has been used here, has been proven to be well suited for diffuse tomography, see for example [29, 35]. As explained in Section 3.2, the prior model is proper; that is, it has finite covariances. Furthermore, by construction, the model can accommodate an unknown background conductivity.

The MAP-CEM reconstruction in which the incorrect model domain is used but the approximation error is not accounted for, shows intolerable errors. In contrast, the MAP-AEM reconstruction in which the approximation errors are accounted for, is mostly free of these artifacts and is comparable to the conventional reconstruction in the correct domain. The shape of domain Ω also has been found quite well, and moreover, the posterior spread estimates are feasible. In addition to the reconstruction of the shapes of the organs, the actual conductivity values also match the reality quite well.

In addition to the Case 1, we conducted tests using several different target chest domains. The results for a difficult case (Case 2) are shown in Fig. 6 and Table 2. The results were computed with exactly the same models and settings,

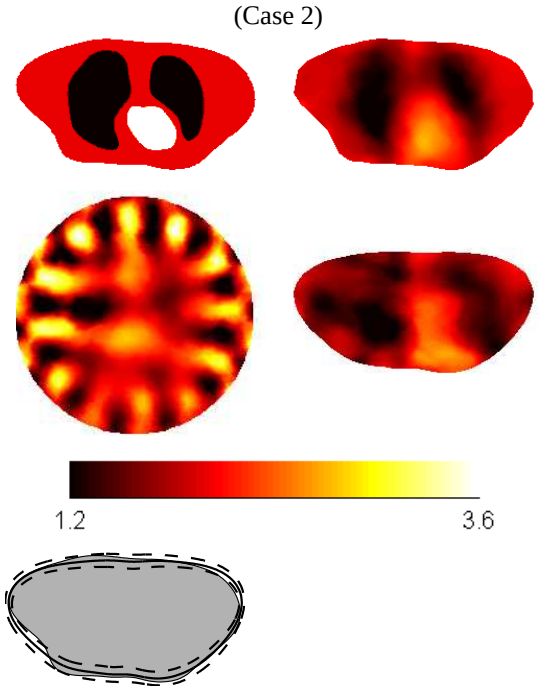

FIG. 6: Results for case 2. Arrangement of images is similar as in Fig. 5.

TABLE 2: The relative estimation errors (Case 2).

Estimate	Forward model	Δ_σ
MAP-CEM	$U(\bar{\sigma},\gamma)$	20.25
MAP-CEM	$U(\sigma,\tilde{\gamma})$	44.47
MAP-AEM	$U(\sigma,\tilde{\gamma})$	25.26

and the images are organized similarly as the results for Case 1 in Fig. 5. The central difference between Cases 1 and 2 is that whereas actual domain Ω in Case 1 is plausible with respect to sample-based prior model $\pi(\gamma)$, the actual domain in Case 2 has low probability with respect to the sample-based prior (see Fig. 2). As can be seen, the MAP-CEM using the incorrect model domain again shows intolerable errors. The MAP-AEM, on the other hand, has still succeeded in recovering the conductivity and the domain shape to some extent, but the degradation compared to the reference estimate (MAP-CEM using the correct domain) is evident and the usefulness of the estimate is questionable. This gives us some indication of the limits of the MAP-AEM approach; the performance (obviously) depends on the prior models that are used and, roughly speaking, one can expect poor estimates whenever the actual domain is improbable with respect to the prior model.

Note that in the present implementation we made the technical approximation that $(\varepsilon,\sigma,e,\gamma)$ are mutually uncorrelated. This assumption cannot be sustained in principle since a perturbation of the boundary effects indirectly also the conductivity via the mapping P [see Eqs. (19)–(20)] and ε is a function of the random variables (σ,γ). However, based on the results this technical approximation seems to be acceptable in practice.

5. TEST CASE USING EXPERIMENTAL DATA AND 3D FEM MODEL

5.1 Experimental Setup

The experimental data were measured from a vertically symmetric measurement tank Ω (see the top left in Fig. 8). Sixteen equally spaced stainless steel electrodes were attached on boundary $\partial\Omega$ of the tank. The (incorrect) model

domain $\tilde{\Omega}$ was a cylinder with a diameter equivalent to the diameter of the measurement domain (see Fig. 7). The height of tank Ω and model domain $\tilde{\Omega}$ was 5 cm. Thus, no model error caused by truncation of the computational domain in the vertical direction was present. To construct the phantom, heart- and lung-shaped inclusions were made of agar and placed in the measurement tank filled with saline with a conductivity of 3.0 mS/cm^{-1}. The inclusions were constructed using vertically symmetric molds. The conductivity of the lung and heart targets were 0.73 mS/cm^{-1} and 5.8 mS/cm^{-1}, respectively.

The measurements were carried out with the KIT 4 measurement system [52]. Sixteen adjacent current patterns were used and the voltage differences between the adjacent electrodes were used as measurements, leading to 256 voltage measurements. The amplitude of the injected currents was 5 mA with a frequency of 10 kHz.

For the estimation of measurement error statistics, 40,000 realizations were measured. The distribution of the measurement noise conformed well with the Gaussian model. The means $e_{*,k}$ and covariances $\Gamma_{e,k}$ were formed separately as sample averages for each of the $k = 1, \ldots, 16$ current patterns. In KIT 4, different current patterns use partially different circuit boards and have different switch states, which may result in different measurement error statistics for different current patterns. Significant external low-frequency sources were not present, and the serial autocorrelation was verified to essentially vanish after the zeroth lag. Thus, the errors in the demodulated voltages could be modeled as mutually independent between current patterns and overall covariance Γ_e was constructed as a block diagonal matrix,

$$\Gamma_e = \mathrm{BlockDiag}(\Gamma_{e,1}, \ldots, \Gamma_{e,16})$$

The standard deviations $[\mathrm{diag}(\Gamma_e)]^{1/2}$ of the noise were in the range from 0.01% to 2.64% of the mean of the measured voltages and the SNR computed as

$$\mathrm{SNR} = 10 \ln \left(\frac{E\{|| V ||^2\}}{\frac{1}{m}\mathrm{tr}(\Gamma_e)} \right) \tag{35}$$

was 65.52 dB. The structure of (essentially) nonzero elements in estimates $\Gamma_{e,k}$ was tridiagonal, implying that the three voltage difference measurements (between adjacent electrode pairs) that involve electrode ℓ are correlated.

Prior $\pi(\bar{\sigma})$ for the 3D model was constructed similarly as for the 2D model explained in Section 3.2. The correlation length in the prior model was set to 7 cm as in the simulation case. The other prior parameters were set as follows. The prior mean was set to the conductivity of the saline background; that is, $\sigma_* = 3.0$ mS/cm^{-1}, $\mu_{\mathrm{in}} = 0.6$ mS/cm^{-1}, and $\mu_{\mathrm{hg}} = 0.15$ mS/cm^{-1}. The correlation length of 7 cm in a 5-cm-tall tank means that (according to the prior model) the conductivities on the bottom and top layers are almost mutually independent. These choices mean, in particular, that we assume that the background conductivity is between $(2.5, 3.5)$ with approximately 99% probability.

The statistics of the modeling errors was again estimated using $N_s = 1000$ conductivity and boundary samples, similarly as explained in Section 3.3. The conductivity samples were drawn from the 3D prior model. The cross sections of the (vertically symmetric) boundary samples were the samples that were used in the 2D case.

Estimates for contact impedances z and homogeneous initialization for the conductivity were computed before the actual reconstruction by solving the least-squares problem

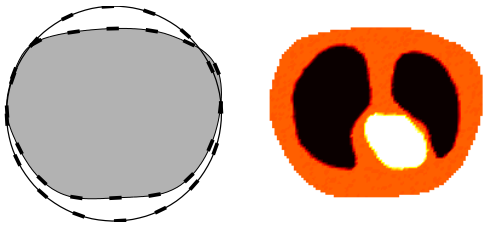

(Case 3; real data)

FIG. 7: Left: The cross section of the actual domain Ω is shown as gray patch. The shape of the domain was extracted from a segmented CT image of the thorax. The cross section of the cylindrical model domain $\tilde{\Omega}$ is shown as solid line. The locations of the 16 electrodes attached on the boundaries are shown with line segments. Right: Arrangement of lung and heart phantoms in the measurement tank.

$$(\sigma_0, z) = \arg \min_{\sigma_0>0, z>0} \left\{ \| L[V - U(\sigma_0, z, \gamma_0) - n_*] \|^2 \right\} \tag{36}$$

where $\sigma_0 \in \mathbb{R}$ is a homogeneous conductivity value and $z \in \mathbb{R}^{16}$ are the electrode contact impedances. Parameters γ_0 are fixed to correspond to the model; that is, $\gamma_0 = \gamma$ when using correct domain Ω and $\gamma_0 = \tilde{\gamma}$ when using model domain $\tilde{\Omega}$ in the forward model. Likewise, mean n_* of the total additive errors and Cholesky factor L depend on the estimate, with $n_* = e_*,\ L = L_e$ when computing initial estimates with the conventional error model (MAP-CEM) and $n_* = e_* + \varepsilon_*,\ L = L_{e+\varepsilon}$ when computing initial estimates with the approximation error approach (MAP-AEM). Similar least-squares approaches for estimation of contact impedances have been proposed in [25, 53, 54].

5.2 Reconstructions Using Experimental Data (Case 3)

The reconstructions of Types 1–3 described in Section 3.1 are shown in Fig. 8, together with a photograph of the measurement phantom. The images that are shown are the central horizontal cross sections of the reconstructed 3D conductivity; that is, 2.5 cm from both the top and bottom layers.

The characteristics of the reconstructions in Fig. 8 are similar to those with Case 1 shown in Fig. 5. Again, the MAP-AEM using incorrect model domain $\tilde{\Omega}$ is able to capture the domain shape and geometry of the organs well,

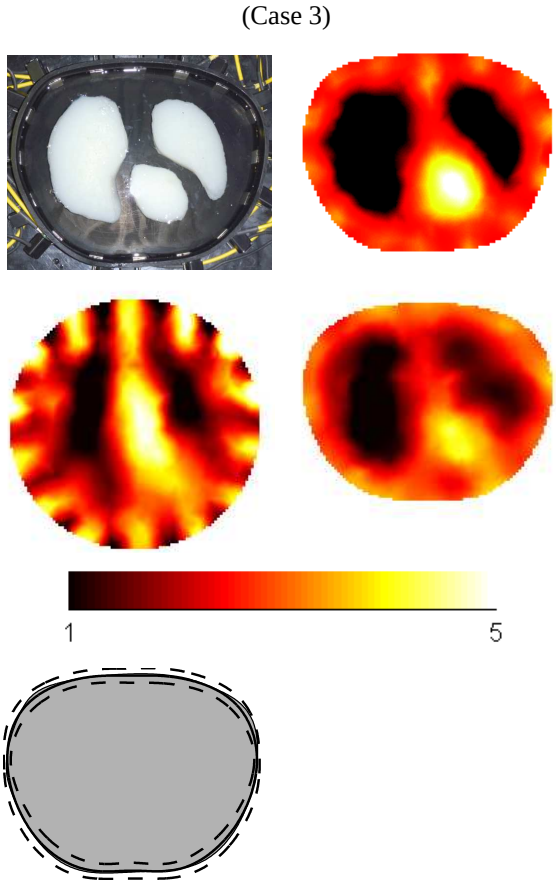

FIG. 8: Top left: The measurement tank. Top right: MAP-CEM estimate using the correct domain Ω. Middle left: MAP-CEM using the incorrect model domain $\tilde{\Omega}$. Middle right: MAP-AEM using the incorrect model domain $\tilde{\Omega}$. The images show the central horizontal cross sections from the 3D reconstructions. Bottom: The cross section of the actual domain Ω is shown as gray patch. The reconstructed boundary is shown with solid line and 2 (*a posteriori*) standard deviation limits with dashed lines.

producing almost as good a reconstruction as the conventional reference estimate (MAP-CEM) that is computed using correct domain Ω. The electrode artifacts that are visible in both the MAP-CEM reference estimate using the correct domain and the MAP-AEM reconstruction are due to the errors in the estimated contact impedances in Eq. (36); values of the contact impedances that are too large have been compensated by an increase in conductivity underneath the electrodes, and vice versa.

6. CONCLUSIONS

In this paper, we considered electrical impedance tomography and the recovery from are incorrectly modeled boundary shape. An incorrectly modeled boundary has been known to induce significant errors to the estimates, typically making absolute EIT imaging impossible in the clinical setting. We applied the recently proposed approximation error approach to the modeling of the errors induced by the unknown boundary shape and approximate reconstruction of the boundary shape. The approximation error approach is based on the Bayesian framework for statistics, in which statistical models for all unknowns and uncertainties, or prior models, are constructed. In this approach, the approximate statistics of the modeling errors are computed over the prior models, and the likelihood model is formulated accordingly. We formulated the approximation error approach in a novel way such that, in addition to the primary unknowns (conductivity), also a low-rank approximation for the realization of the modeling error is estimated and then used for approximate recovery of the domain boundary.

We considered both simulation examples as well as a real tank measurement case, corresponding to a thorax imaging problem. For the construction of the prior distribution for the thorax shape, CT images were used. The results show that the proposed approach is well suited for the recovery from uncertainty in the boundary shape, allowing feasible reconstructions of both the conductivity and domain boundary when the prior models are plausible. Moreover, the posterior spread estimates for the uncertainty in the boundary shape are also feasible.

In biomedical applications of EIT, the boundary shape is seldom known to the accuracy required by absolute imaging. The results of this paper, together with earlier results concerning the handling of the truncation of the computational domain, suggest that absolute EIT imaging might be a clinically relevant possibility.

ACKNOWLEDGMENTS

The work was supported by the Academy of Finland projects 119270, 140731 and 213476, Finnish Centre of Excellence in Inverse Problems Research 2006-2011.

REFERENCES

1. Zou, Y. and Guo, Z., A review of electrical impedance techniques for breast cancer detection, *Med. Eng. Phys.*, 25:79–90, 2003.
2. Boverman, G., Kao, T.-K., Kulkarni, R., Kim, B. S., Isaacson, D., Saulnier, G. J., and Newell, J. C., Robust linearized image reconstruction for multifrequence eit of the breast, *IEEE Trans. Med. Im.*, 27:1439–1448, 2008.
3. Tidswell, A. T., Gibson, A., Bayford, R. H., and Holder, D. S., Validation of a 3d reconstruction algorithm for eit of human brain function in a realistic head-shaped tank, *Physiol. Meas.*, 22:117–185, 2001.
4. I.Frerichs, Electrical impedance tomography (eit) in applications related to lung and ventilation: a review of experimental and clinical activities, *Physiol. Meas.*, 21:R1–R21, 2000.
5. Frerichs, I., Hinz, J., Herrmann, P., Weisser, G., Hahn, G., Dudykevych, T., Quintel, M., and Hellige, G., Detection of local lung air content by electrical impedance tomography compared with electron beam ct, *J. Appl. Physiol*, 93:660–666, 2002.
6. Victorino, J., Borges, J. B., Okamoto, V. N., Matos, G. F. J., Tucci, M. R., Caramez, M. P. R., Tanaka, H., Sipmann, F. S., Santos, D. C. B., Barbas, C. S. V., Carvalho, C. R. R., and Amato, M. B. P., Imbalances in regional lung ventilation, *Am. J. Respir. Crit. Care. Med.*, 169:791–800, 2004.
7. Cheney, M., Isaacson, D., and Newell, J. C., Electrical impedance tomography, *SIAM Rev*, 41:85–101, 1999.
8. Kaipio, J. P., Kolehmainen, V., Somersalo, E., and Vauhkonen, M., Statistical inversion and Monte Carlo sampling methods in electrical impedance tomography, *Inv. Probl.*, 16:1487–1522, 2000.

9. Brown, B. H., Electrical impedance tomography (eit): a review, *J. Medical Eng. Tech.*, 27(3):97–108, 2003.
10. Gersing, E., Hoffmann, B., and Osypka, M., Influence of changing peripheral geometry on electrical impedance tomography measurements, *Med. Biol. Eng. Comput.*, 34:359–361, 1996.
11. Kolehmainen, V., Vauhkonen, M., Karjalainen, P. A., and Kaipio, J. P., Assessment of errors in static electrical impedance tomography with adjacent and trigonometric current patterns, *Physiol. Meas.*, 18:289–303, 1997.
12. Jain, H., Isaacson, D., Edic, P. M., and Newell, J. C., Electrical impedance tomography of complex conductivity distributions with noncircular boundary, *IEEE Trans. Biomed. Eng.*, 44:1051–1060, 1997.
13. Zhang, J. and Pattersson, R. P., Eit images of ventilation: what contributes to the resistivity changes?, *Physiol. Meas.*, 26:S81–S92, 2005.
14. Tossavainen, O. P., Vauhkonen, M., Heikkinen, L. M., and Savolainen, T., Estimating shapes and free surfaces with electrical impedance tomography, *Meas. Sci. Technol.*, 15:1402–1411, 2004.
15. Tossavainen, O. P., Kolehmainen, V., and Vauhkonen, M., Free-surface and admittivity estimation in electrical impedance tomography, *Int. J. Num. Meth. Eng.*, 66:1991–2013, 2006.
16. Barber, D. C. and Brown, B. H., Applied potential tomography, *J. Phys. E: Sci. Instrum.*, 17:723–733, 1984.
17. Adler, A., Guardo, R., and Berthiaume, Y., Impedance imaging of lung ventilation: Do we need to account for chest expansion?, *IEEE Trans. Biomed. Eng.*, 43:414–420, 1996.
18. Hahn, G., Just, A., Dudykevych, T., Frerichs, I., Hinz, J., Quintel, M., and Hellige, G., Imaging pathologic pulmonary air and fluid accumulation by functional and absolute eit, *Physiol. Meas.*, 27:S187–S198, 2006.
19. Costa, E. L. V., Chaves, C. N., Gomes, S., Beraldo, M. A., Volpe, M. S., Tucci, M. R., Schettino, I. A. L., Bohm, S. H., Carvalho, C. R. R., Tanaka, H., Lima, R. G., and Amato, M. B. A., Real-time detection of pneumothorax using electrical impedance tomography, *Crit. Care. Med.*, 36:1230–1238, 2008.
20. Soleimani, M., Comez-Laberge, C., and Adler, A., Imaging of conductivity changes and electrode movement in eit, *Physiol. Meas.*, 27:S103–S113, 2006.
21. Dai, T., Gomez-Laberge, C., and Adler, A., Reconstruction of conductivity changes and electrode movements based on eit temporal sequences, *Physiol. Meas.*, 29:S77–S88, 2008.
22. Nachman, A. I., Global uniqueness for a two-dimensional inverse boundary value problem, *Ann. Math.*, 143:71–96, 1996.
23. Murphy, E. K. and Mueller, J. L., Effect of domain shape modeling and measurement errors on the 2-d d-bar method for eit, *IEEE Trans. Med. Im.*, 28:1576–1584, 2009.
24. Kolehmainen, V., Lassas, M., and Ola, P., The inverse conductivity problem with an imperfectly known boundary, *SIAM J. Appl. Math.*, 66:365–383, 2005.
25. Kolehmainen, V., Lassas, M., and Ola, P., Electrical impedance tomography problem with inaccurately known boundary and contact impedances, *IEEE Trans. Med. Im.*, 27:1404–1414, 2008.
26. Kolehmainen, V., Lassas, M., and Ola, P., The inverse conductivity problem with an imperfectly known boundary in three dimensions, *SIAM J. Appl. Math.*, 67:1440–1452, 2007.
27. Lionheart, W. R. B., Boundary shape and electrical impedance tomography, *Inv. Probl.*, 14:139–147, 1998.
28. Nissinen, A., Kolehmainen, V., and Kaipio, J. P., Compensation of modelling errors due to unknown domain boundary in electrical impedance tomography, *IEEE Trans. Med. Im.*, 30:231–242, 2011.
29. Kaipio, J. P. and Somersalo, E., Statistical and computational inverse problems, in *Applied Mathematical Sciences 160*, Springer-Verlag, 2005.
30. Kaipio, J. P. and Somersalo, E., Statistical inverse problems: Discretization, model reduction and inverse crimes, *J. Comput. Appl. Math.*, 198:493–504, 2007.
31. Nissinen, A., Heikkinen, L. M., and Kaipio, J. P., The bayesian approximation error approach for electrical impedance tomography—Experimental results, *Meas. Sci. Technol.*, 19:015501, 2008.
32. Lehikoinen, A., Finsterle, S., Voutilainen, A., Heikkinen, L. M., Vauhkonen, M., and Kaipio, J. P., Approximation errors and truncation of computational domains with application to geophysical tomography, *Inverse Probl. Imaging*, 1:371–389, 2007.
33. Pursiainen, S., Two-stage reconstruction of a circular anomaly in electrical impedance tomography, *Inv. Probl.*, 22:1689–1703, 2006.

34. Nissinen, A., Heikkinen, L. M., Kolehmainen, V., and Kaipio, J. P., Compensation of errors due to discretization, domain truncation and unknown contact impedances in electrical impedance tomography, *Meas. Sci. Technol.*, 20:105504, 2009.
35. Arridge, S. R., Kaipio, J. P., Kolehmainen, V., Schweiger, M., Somersalo, E., Tarvainen, T., and Vauhkonen, M., Approximation errors and model reduction with an application in optical diffusion tomography, *Inv. Probl.*, 22:175–195, 2006.
36. Kolehmainen, V., Schweiger, M., Nissilä, I., Tarvainen, T., Arridge, S. R., and Kaipio, J. P., Approximation errors and model reduction in three-dimensional diffuse optical tomography, *J. Opt. Soc. Am.*, 26(10):2257–2268, 2009.
37. Heino, J. and Somersalo, E., A modeling error approach for the estimation of optical absorption in the presence of anisotropies, *Phys. Med. Biol.*, 49:4785–4798, 2004.
38. Heino, J., Somersalo, E., and Kaipio, J. P., Compensation for geometric mismodelling by anisotropies in optical tomography, *Opt. Express*, 13:296–308, 2005.
39. Calvetti, D., Kaipio, J. P., and Somersalo, E., Aristotelian prior boundary conditions, *Int. J. Math.*, 1:63–81, 2006.
40. Tarvainen, T., Kolehmainen, V., Pulkkinen, A., Vauhkonen, M., Schweiger, M., Arridge, S. R., and Kaipio, J. P., Approximation error approach for compensating modelling errors between the radiative transfer equation and the diffusion approximation in diffuse optical tomography, *Inv. Probl.*, 26:015005, 2010.
41. Kolehmainen, V., Tarvainen, T., Arridge, S. R., and Kaipio, J. P., Marginalization of uninteresting distributed parameters in inverse problems—Application to optical tomography, *Int. J. Uncertainty Quantification*, 1(1):1–17, 2011.
42. Huttunen, J. M. J. and Kaipio, J. P., Approximation errors in nonstationary inverse problems, *Inverse Probl. Imaging*, 1:77–93, 2007.
43. Huttunen, J. M. J. and Kaipio, J. P., Approximation error analysis in nonlinear state estimation with an application to state-space identification, *Inv. Probl.*, 23:2141–2157, 2007.
44. Voutilainen, A. and Kaipio, J. P., Model reduction and pollution source identification from remote sensing data, *Inv. Probl. Imaging*, 2:711–730, 2009.
45. Cheng, K.-S., Isaacson, D., Newell, J. C., and Gisser, D. G., Electrode models for electric current computed tomography, *IEEE Trans. Biomed. Eng.*, 36:918–924, 1989.
46. Somersalo, E., Cheney, M., and Isaacson, D., Existence and uniqueness for electrode models for electric current computed tomography, *SIAM J. Appl. Math.*, 52:1023–1040, 1992.
47. Vauhkonen, P. J., Vauhkonen, M., Savolainen, T., and Kaipio, J. P., Three-dimensional electrical impedance tomography based on the complete electrode model, *IEEE Trans. Biomed. Eng.*, 46:1150–1160, 1999.
48. Calvetti, D. and Somersalo, E., *An Introduction to Bayesian Scientific Computing—Ten Lectures on Subjective Computing*, Springer, New York, 2007.
49. Tarantola, A., *Inverse Problem Theory and Methods for Model Parameter Estimation*, SIAM, Philadelphia, 2004.
50. Nocedal, J. and Wright, S. J., *Numerical Optimization (second edition)*, Springer, New York, 2006.
51. Goshtasby, A., *2-D and 3-D Image Registration for Medical, Remote Sensing, and Industrial Applications*, Wiley, Hoboken, NJ, 2005.
52. Kourunen, J., Savolainen, T., Lehikoinen, A., Vauhkonen, M., and Heikkinen, L. M., Suitability of a pxi platform for an electrical impedance tomography system, *Meas. Sci. Technol.*, 20:015503, 2009.
53. Heikkinen, L. M., Vilhunen, T., West, R. M., and Vauhkonen, M., Simultaneous reconstruction of electrode contact impedances and internal electrical properties: Ii. laboratory experiments, *Meas. Sci. Technol.*, 13:1855–1861, 2002.
54. Vilhunen, T., Kaipio, J. P., Vauhkonen, P. J., Savolainen, T., and Vauhkonen, M., Simultaneous reconstruction of electrode contact impedances and internal electrical properties: I. theory, *Meas. Sci. Technol.*, 13:1848–1854, 2002.